




A wideband biconic shape metasurface for polarization conversion and radar cross-section reduction

Haseeba Kanwal¹, Babar Kamal² , Sadiq Ullah¹, Waleed Shihzad¹, Usman Ali¹, Amjad Aziz¹ and Zakriya Faraz¹

¹Department of Telecommunication Engineering, University of Engineering and Technology, Mardan, Khyberpukhtoonkhwa, Pakistan and ²Center of Intelligent Acoustics and Immersive Communications, Northwestern Polytechnical University, Xi'an, Shaanxi, China

Research Paper

Cite this article: Kanwal H, Kamal B, Ullah S, Shihzad W, Ali U, Aziz A, Faraz Z (2024) A wideband biconic shape metasurface for polarization conversion and radar cross-section reduction. *International Journal of Microwave and Wireless Technologies* **16**(10), 1685–1695. <https://doi.org/10.1017/S175907872400059X>

Received: 14 January 2024
Revised: 15 May 2024
Accepted: 16 May 2024

Keywords:

angular sensitivity; fractional bandwidth; linearly polarized; metasurface; phase cancellation; Polarization; polarization conversion; radar cross section; wideband

Corresponding author: Babar Kamal;
Email: babarkamal.55@mail.nwpu.edu.cn

Abstract

A single-layer polarization converting metasurface (PCMS) with wideband is presented for polarization conversion and radar cross-section (RCS) reduction. The proposed PCMS is composed of metallic biconic shape resonator imprinted on a metal-backed F4BM dielectric substrate of relative permittivity 2.2 and loss tangent 0.001. The unit cell has a compact size of $0.16\lambda_0 \times 0.16\lambda_0$. A comprehensive parametric analysis, angular sensitivity study, bistatic and monostatic RCS analysis are conducted by illuminating the proposed PCMS using linearly polarized (LP) plane waves. The PCMS converts LP electromagnetic waves to their orthogonal polarization state in the frequency band of 8.7–24.8 GHz resulting in polarization conversion ratio over 90% with a fractional bandwidth of 96%. Additionally, the developed structure is applied in chessboard configuration, using phase cancellation techniques for RCS reduction, that achieve 10 dB RCS reduction across a wideband of 7.9–23.4 GHz. The unit cell and its rotated version has a cross-polarization reflection phase difference of $(180 \pm 37^\circ)$ in the operating band, which fulfill the criteria for RCS reduction. The chessboard configuration exhibits a scattering pattern with four strong lobes that deviates from the normal incident path because of the phase cancellation in normal direction. The experimental results are in good agreement with the simulated result. Applications for the developed structure include antenna design (gain enhancement and beam steering), target hiding, imaging, and microwave communications.

Introduction

Metasurface attract researcher's interest, as it has unique capability of manipulating electromagnetic (EM) wave [1, 2]. Electric (E) field and magnetic (H) field vectors oscillate perpendicularly to each other to form an EM wave. The polarization of the EM wave is usually determined by the E-field [3]. The polarization of EM waves is one of its most fundamental properties. Polarization can be controlled with the help of conventional techniques using natural materials. Some of the conventional methods for controlling polarization include the Faraday effect, the optical activity of crystals [4], solutions of chiral compounds (sugar), and proteins with helical secondary structures [5]. It should be noted that the converter based on the aforementioned techniques has the limitations of narrowband frequency response [6, 7], a thicker and bulkier volume [8], these converters are consequently incompatible with many real-world applications. The planar metamaterials known as metasurfaces are two-dimensional (2D) in nature and can be used for control of polarization, phase, and amplitude of EM waves [9–11]. Metasurfaces (MSs) have many EM applications, and they have been successfully utilized to make high-impedance surfaces [12], lenses [13], invisible cloaks [8], perfect absorbing [14, 15], backward propagation, polarization conversion [16], and antenna systems [17]. The advantages of MSs compared to conventional polarizers are small size, less lossy, wide bandwidth, easy to fabricate, and unique capability to manipulate EM wave, due to these feature MSs are used in many practical applications [8]. Polarization converting metasurface (PCMS) operates in reflection mode and transmission mode as a cross polarizer [18]. There are two ways to design PCMS, one is single layer and the other is multilayer. Recently, several PCMS with a wide bandwidth were reported [19–21] using single-layer method but these PCMSs have the limitation of low efficiency. A PCMS with polarization conversion ratio (PCR) greater than 90% for linearly polarized (LP) waves over a frequency range of 8.2–23 GHz with a fractional bandwidth (FBW) of 95% is presented in [22]. The multilayer PCMSs were also reported to enhance the bandwidth and efficiency but due to its large size and thickness from the single-layer PCMS [23], the fabrication of such multilayer

structure is difficult. However, using single-layer method, a simple structure, high bandwidth, and efficient PCMS are still a difficult task.

EM scattering is the process when an EM wave impinges on an object or a scatterer, the energy carried by the EM wave is deflected in all directions. A fundamental application of MS is EM wave cloaking, which is meant to scatter the EM waves away from radar direction to reduce the detectability of targets.

Radar cross-section (RCS) reduction is the fundamental issue of stealth technologies. To lower the RCS of the metallic object, several conventional techniques have been proposed such as shape optimization (reshaping) [24] and radar absorbing materials (RAMs) [25]. Reshaping is a standard strategy for lowering RCS, by changing the target geometry or by eliminating conductors that don't contribute to the radiation characteristics, by maintaining its radiation performance, RCS reduction is achieved but the drawback of shape optimization is that the geometry of the object is changed. As for the RAMs, it converts the incident EM wave energy into heat to camouflage targets, but the increasing body temperatures are challenging. An additional method for RCS reduction consists of organizing perfect electric conductor (PEC) and artificial magnetic conductor surfaces in checkerboard structures in order to redirect the reflected waves into other directions [26, 27]. In contrast, the conventional methods mentioned above have the disadvantages of either being difficult to design or bulky, narrow in bandwidth [3], computationally expensive, and time-consuming, which have some applications and limitations. Another method for RCS reduction using PCMS has been presented in recent decades. In which the PCMS and its mirror PCMS are placed in various chessboard arrangements, having a cross-polarization phase difference of $(180 \pm 37^\circ)$ between the PCMS and its mirror PCMS. In Ref. [28], a polarization converter has 90% PCR from 9.2 to 17.7 GHz and it achieved -10 dB RCS reduction in the same band. In Ref. [29], a PCMS exhibits PCR higher than 60% in the 8.4–11.1 GHz frequency range and -10 dB RCS reduction from 8 to 13 GHz. In Ref. [30], the RCS is reduced from 7.85 to 12.25 GHz as a result of the $180^\circ \Delta\varphi$ between the PCMS and its mirror PCMS. However, -10 dB RCS reduction across wideband is still difficult to achieve. Our research focuses on designing a wideband and high efficient polarization converter for RCS reduction.

In this study, a PCMS is designed to obtain more than 90% PCR in a wideband for RCS reduction. The designed PCMS converts linear polarized wave to its orthogonal state. To analyze the backscattered fields, the proposed PCMS is organized in chessboard orientations to understand its RCS reduction capability. According to the simulation results, the proposed design has a 10 dB monostatic RCS reduction from 7.9 to 23.4 GHz as compared to an identical sized PEC. The proposed design is validated by the experimental results, which exhibit a strong correlation with the simulation results.

Unit cell configuration

The designed unit cell consists of three layers, the top layer is metallic biconic shape imprinted onto a dielectric substrate which is middle layer and its bottom layer is metallic ground. All the metallic layers (top and bottom) are modeled as copper having electrical conductivity $\sigma = 5.8 \times 10^7$ S/m and each having a 0.035 mm thickness. The F4BM dielectric substrate $\epsilon_r = 2.2$, $\tan\delta = 0.001$ separates both metallic layers from each other. The designed unit cell was simulated, and its performance was evaluated using a frequency domain solver in CST Microwave Studio

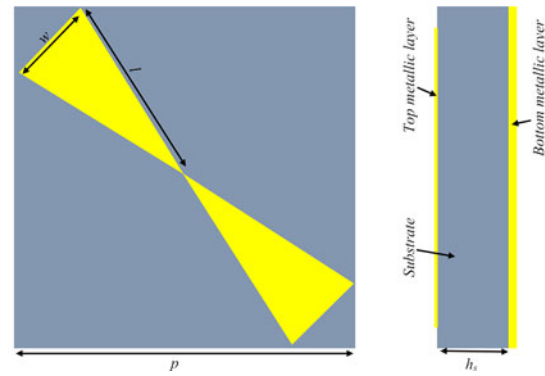


Figure 1. Configuration of the biconic shape PCMS.

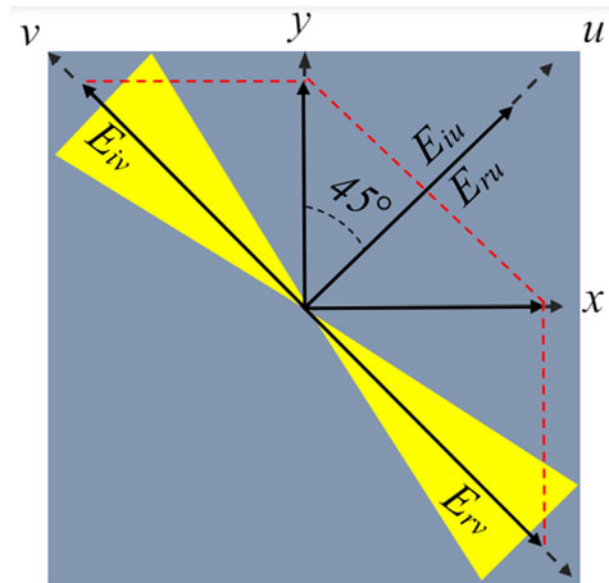


Figure 2. The designed PCMS u - v decomposition.

2020. The periodic boundary condition was applied along the x - and y -directions to make an infinite periodic array and the open boundary condition was applied in z -direction. Figure 1 illustrates the designed unit cell geometry, with the following parameters: $p = 5.6$ mm, $h_s = 3$ mm, $w = 1.45$ mm, and $l = 3.16$ mm.

Simulation results and discussions

Using the finite element approach, the proposed design was simulated to assess its polarization conversion performance. Due to the asymmetry of the proposed PCMS, when an EM wave with a particular polarization state imposes on it, the reflected EM wave contains co- and cross-polarized components. In terms of reflection coefficients, co-polarized reflection amplitude is $r_{yy} = |E_{yr}|/|E_{yi}|$, and the cross-polarization reflection amplitude is $r_{xy} = |E_{xr}|/|E_{yi}|$, the subscript i stands for incident, and r for reflected EM wave, whereas the subscripts x and y show the axis in which the E-field is polarized.

The incident y -polarized wave is split into u - and v -components as indicated in Figure 2, to better comprehend the cross-polarization conversion mechanism. The incident E-field is described by [31]:

$$\vec{E}_i = u\vec{E}_{iu} + v\vec{E}_{iv}. \quad (1)$$

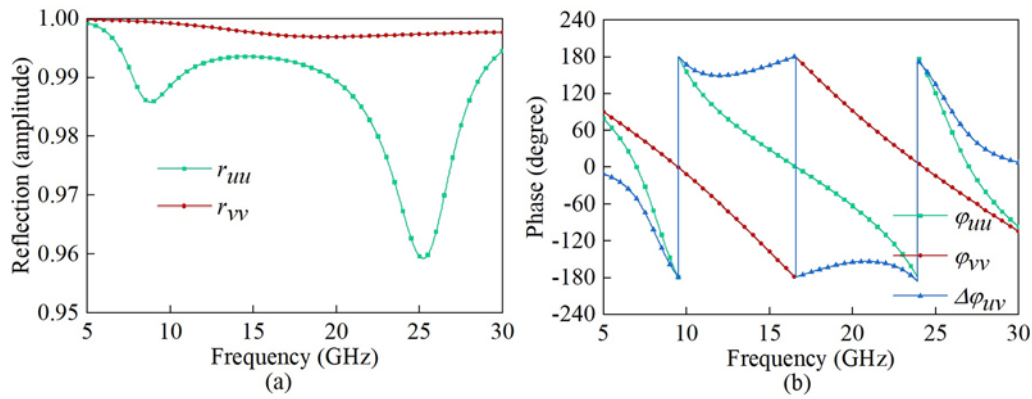


Figure 3. Simulated u - and v -polarized waves: (a) reflection amplitude and (b) phase difference.

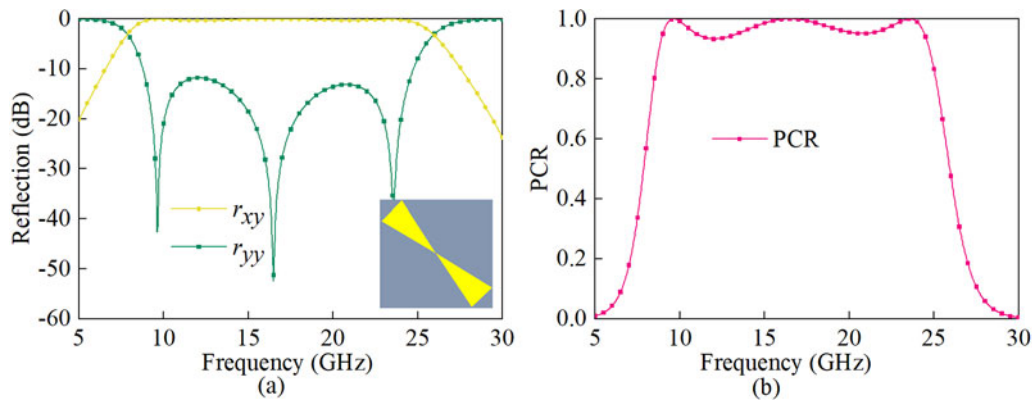


Figure 4. Simulated results of (a) Reflection amplitude for y -polarized wave and (b) PCR.

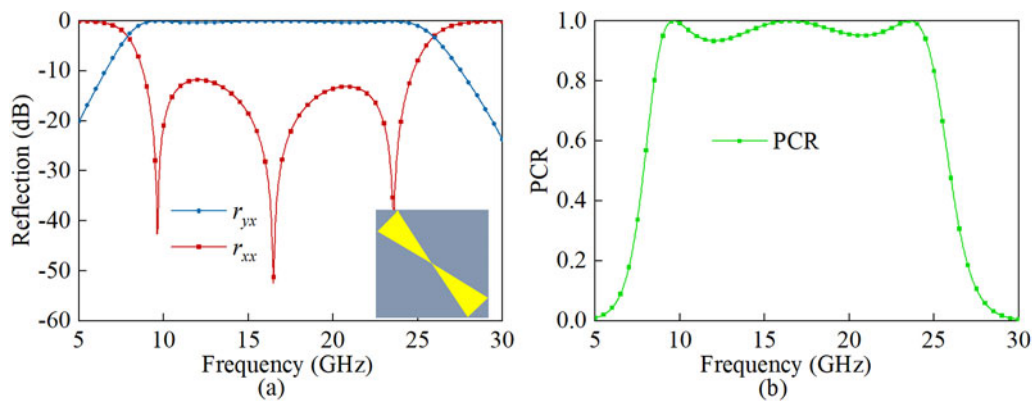


Figure 5. Simulated results of (a) Reflection amplitude for x -polarized wave and (b) PCR.

The reflected E-field can be defined by [31]:

$$\vec{E}_r = u \tilde{r}_u \vec{E}_{iu} + v \tilde{r}_v \vec{E}_{iv}. \tag{2}$$

The reflection amplitudes along the u -axis are represented by the symbol \tilde{r}_u , while those along the v -axis are represented by the symbol \tilde{r}_v , respectively. As the proposed PCMS is an anisotropic nature, which produce a $\Delta\varphi$ between \tilde{r}_u and \tilde{r}_v . If $r_u \approx r_v \approx 1$ and $\Delta\varphi$ approaches 180° , then the surface will change polarization of LP incident EM wave (i.e., x -polarized to y -polarized and vice versa). Figure 3(a) and (b) illustrates reflection amplitude, phases,

and the $\Delta\varphi$ between u - and v -polarized waves, which shows that a linear polarization conversion is achieved because the amplitudes are so close to one another (i.e., $r_u \approx r_v$) and the $\Delta\varphi \approx 180^\circ$. There is no doubt about the metasurface capacity to transform polarization over a wide frequency band of 16.1 GHz. The polarization transformation efficiency of the PCMS is determined from PCR, which is described as [31]:

$$\text{PCR} = \frac{|r_{yx}^2|}{|r_{yx}^2| + |r_{xx}^2|} = \frac{|r_{xy}^2|}{|r_{xy}^2| + |r_{yy}^2|}. \tag{3}$$

If $\text{PCR} = 1$, it means that an LP EM wave is fully converted into its orthogonal equivalent. For y -polarized EM wave,

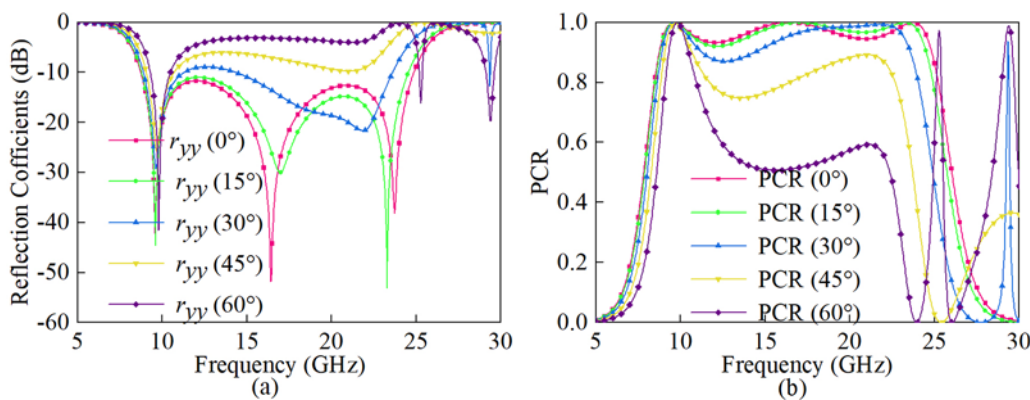


Figure 6. Angle sensitivity of the proposed PCMS: (a) reflection coefficients and (b) PCR with varied angles from 0° up to 60°.

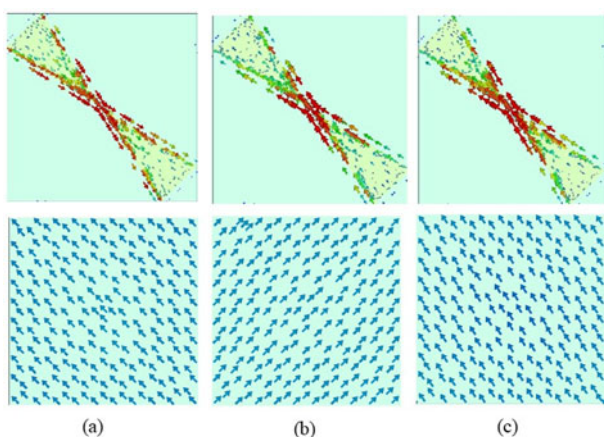


Figure 7. Distribution of surface current on the top and bottom layer of PCMS: (a) 9.6, (b) 16.4, and (c) 23.1 (all in GHz).

the reflection amplitudes are depicted in Figure 4(a), which shows that it is less than -10 dB from 8.7 to 24.8 GHz with an FBW of 96%. The reflected coefficients at *x*-polarized incidence is shown in Figure 5(a). For the proposed PCMS, the cross- and co-polarization reflection coefficients at *x*- and *y*-polarized incidences, i.e., $r_{yy} = r_{xx}$ and $r_{xy} = r_{yx}$ are equal. The response of the MS is same for both *x*- and *y*-polarized EM waves due to the symmetric structure of the unit cell in the *xy* plane.

Furthermore, both the *y*- and *x*-polarized reflection coefficients show the existence of three resonance frequencies at 9.6, 16.4, and 23.1 GHz. Figure 4(b) and 5(b) display the PCR of the proposed PCMS for *y*- and *x*-polarized EM wave, which indicates that in the operating band of 8.7–24.8 GHz, the proposed PCMS has a PCR of greater than 90%. Moreover, the PCR is 100% at 9.6, 16.4, and 23.1 GHz.

There are numerous applications that need the stability of the PCMS performance when the EM wave hits it from varied angles. To test the angular stability of the design PCMS, numerical simulations are done for oblique incidence with theta ranging from 0° to 60°. The simulated reflection coefficients and PCR for oblique incident angles are shown in Figure 6. The proposed MS retains more than 85% PCR from 8.7 to 24.8 GHz up to a 30° incidence angle as shown in Figure 6(b). Furthermore, the PCR and bandwidth of the proposed MS decrease, with increasing incidence angle beyond 30°. The proposed MSs have 100% PCR for all the incident angles from 9.5 to 10 GHz.

To comprehend the proposed biconic shape polarization converter’s physical mechanism, the surface current analysis has been done at resonance frequencies of 9.6, 16.4, and 23.1 GHz as illustrated in Figure 7. Surface currents are seen to be generated at the upper and lower layer of the MS due to the propagation of EM wave [32]. It is clearly seen that at 9.6 and 16.4 GHz, the direction currents are anti-parallel on the metallic patch and ground of the PCMS as shown in Figure 7(a) and (b), which produces significant magnetic resonance by producing a circulating field

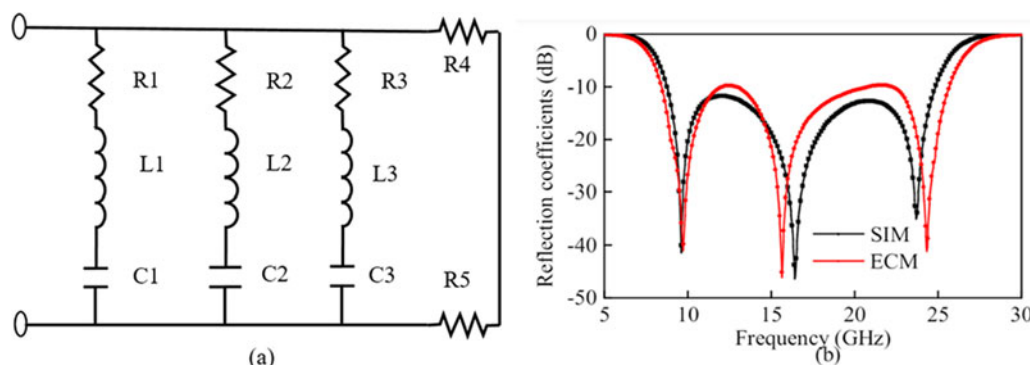


Figure 8. Depiction of (a) Equivalent circuit model and (b) comparison between the numerical simulation (CST) and circuit simulation (ADS).

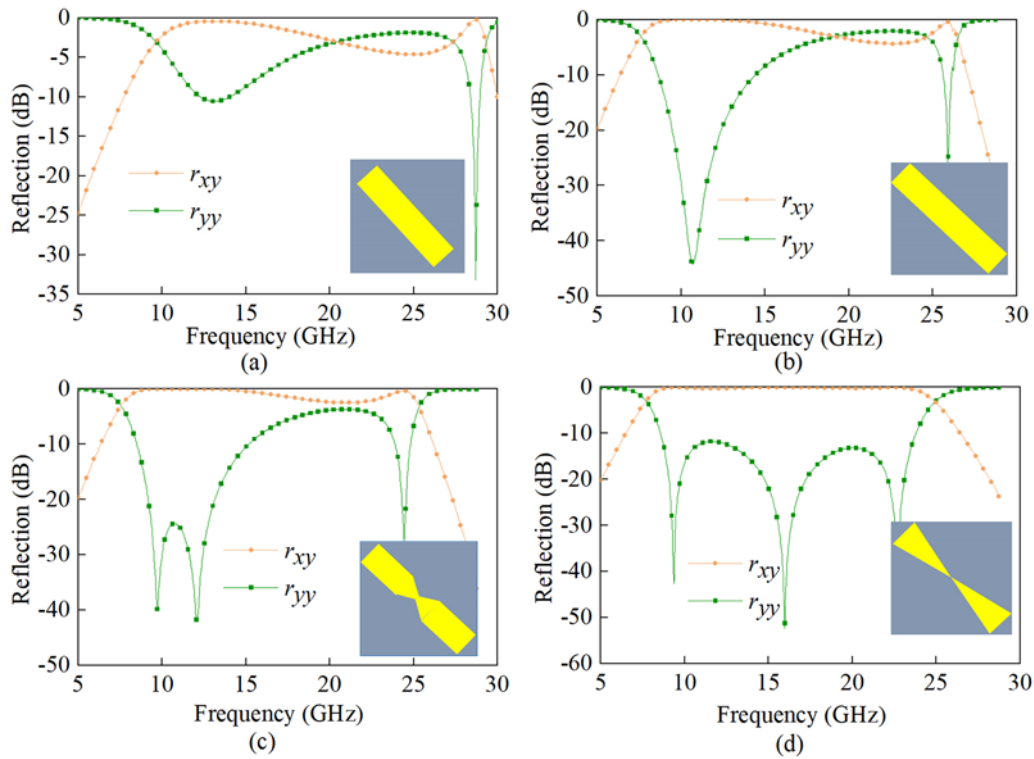


Figure 9. The evaluation steps and simulation results of the proposed PCMS.

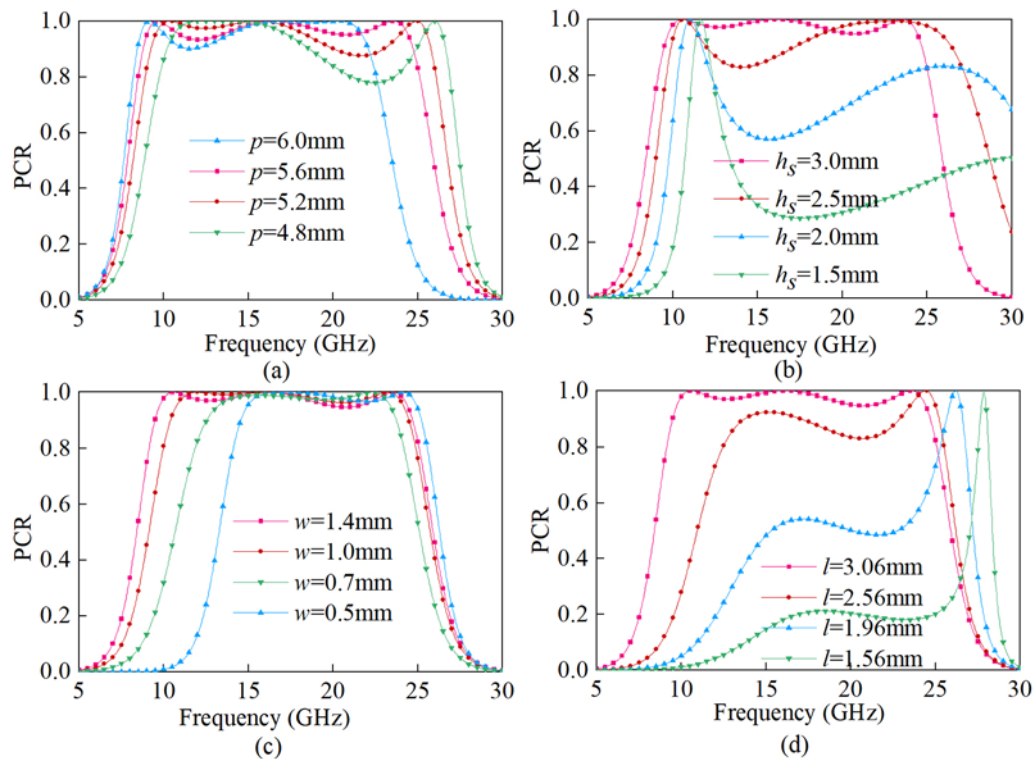


Figure 10. Parametric analysis of the proposed unit cell with respect to various parameters: (a) length and width of substrate (p), (b) thickness of substrate (h_s), (c) width of patch (w), and (d) length of patch (l).

around the incident H-field. This phenomenon increases magnetic permeability, causing the effective surface impedance of the MS to increase and exceed then free space impedance. So, at

resonance frequencies of 9.6 and 16.4 GHz, the impedance of the surface increases. Figure 7(c) illustrates that the current directions in the two metallic layers of the PCMS are the same (parallel)

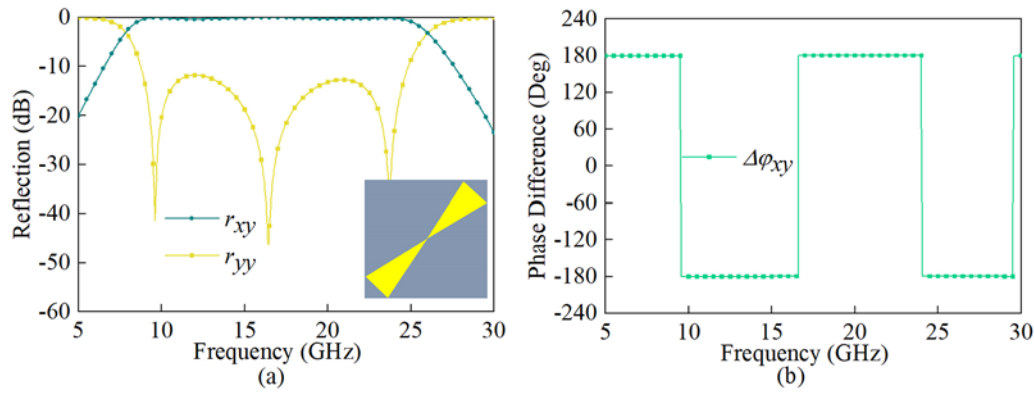


Figure 11. Simulated results: (a) reflection amplitude of mirror version and (b) cross-polarization reflections $\Delta\varphi$ between the proposed unit cell and its mirror version.

at 23.1 GHz, resulting in electric dipole resonance. Therefore, at this resonance frequency, the surface behaves as a PEC, resulting in cross-polarization conversion. Three plasmon resonances are excited by the aforementioned electrical and magnetic resonances, and they provide the basis for the metasurface's operational principle. The presence of electric and magnetic resonances provides a wide bandwidth as well as a high PCR of the MS. The equivalent circuit of the proposed biconic shape PCMS has been modeled using a transmission line model. The unit cell is represented by three series RLC resonant circuit connected in parallel corresponding to three neighboring superimposed resonant peaks in the polarization conversion band [33] as shown in Figure 8(a). The metallic resonator is represented by series inductors ($L1$, $L2$, and $L3$) and resistors ($R1$, $R2$, and $R3$). Meanwhile, the dielectric substrate is represented by capacitors ($C1$, $C2$, and $C3$) and resistors ($R4$, and $R5$), and the ground metal plate is represented by a short-circuited transmission line [34]. The values of inductors and capacitors are calculated by using the following formulas:

$$L = \frac{\mu_o \mu_r LW}{hc} \quad (4)$$

$$C = \frac{\epsilon_o \epsilon_r LW}{hs} \quad (5)$$

where L and W are length and width of metal are taken with the help of surface currents mentioned in Figure 7(a–c), respectively, while hs and hc are thickness of dielectric substrate and metallic conductor, and μ_r is relative permeability of surrounding material, and ϵ_r is relative permittivity of dielectric material. The calculated and extracted parameters values from ADS are as follows: $R1 = 0.9 \Omega$, $R2 = 0.5 \Omega$, $R3 = 0.9 \Omega$, $R4 = 25 \Omega$, $R5 = 25 \Omega$, $L1 = 1.25$ nH, $L2 = 1$ nH, $L3 = 1.3$ nH, $C1 = 0.2$ pF, $C2 = 0.099$ pF, $C3 = 0.032$ pF. The reflection coefficient obtained by ADS and CST are compared and shown in Figure 8(b) which validates the equivalent circuit model.

Simulation steps and variation in geometric parameters

The first step to design a PCMS is to choose the dimensions of the MS to achieve the resonances at desired frequency band [35]. The following equation can be used to compute an approximate estimate of the resonances

$$C = n\lambda_{\text{eff}} = \frac{nc}{f\sqrt{\epsilon_{\text{eff}}}} \quad (6)$$

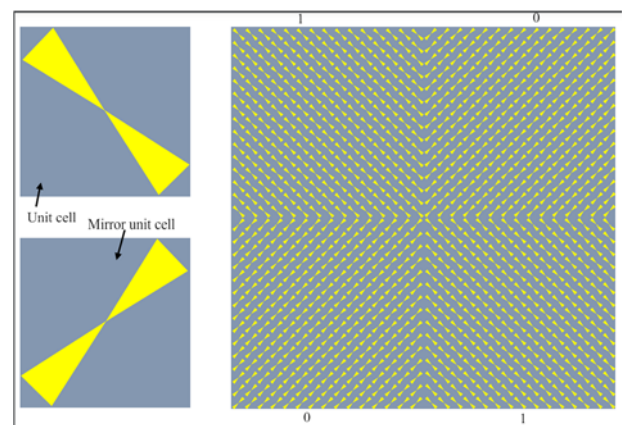


Figure 12. The proposed square chessboard array made up of unit cell and its mirror unit cell.

where C is the circumference of the circle or the largest dimension of the patch and ϵ_{eff} is the effective permittivity [35]. λ_{eff} is the effective wavelength, c is the wave velocity in vacuum, and f is the resonance frequency. To achieve magnetic resonance, n should be considered unity. On the other hand, the electric resonances are achieved for $n = 2$ [35]. Four major steps are taken to create the proposed biconic shape design as shown in Figure 9. In step 1, depicted in Figure 9(a), a rotated rectangular patch is simulated with geometric parameters of $p = 5.6$ mm, $h_s = 3$ mm, $w = 1.45$ mm, and $l = 5.60$ mm, which shows that polarization conversion occur from 10 to 16 GHz and at 28 GHz. In step 2, the length of the rotated rectangular patch is increased in upward and downward direction equally such that the l becomes 6.32 mm, as shown in Figure 9(b). Dual-band polarization conversion occur from 8 to 18 GHz and 28 to 29 GHz. In step 3, some of the rotated rectangular patch parts are removed to create a shape resembling a sand clock, in this sand clock the smaller edge l near the center is 1.07 and the other length is 2.60 as shown in Figure 9(c), polarization conversion occurs from 9 to 19 GHz and at 25 GHz. In step 4, the sand clock shape is optimized to form a biconic shape with geometric parameters $p = 5.6$ mm, $h_s = 3$ mm, $w = 1.45$ mm, and $l = 3.16$ mm as shown in Figure 9(d), which result in three plasmon resonances, leading to more efficient polarization conversion through an ultra wideband range of 8.7–24.8 GHz. The surface is correlated at three plasmon resonances by these well-designed steps, resulting in a high efficient and wideband PCMS. For a better

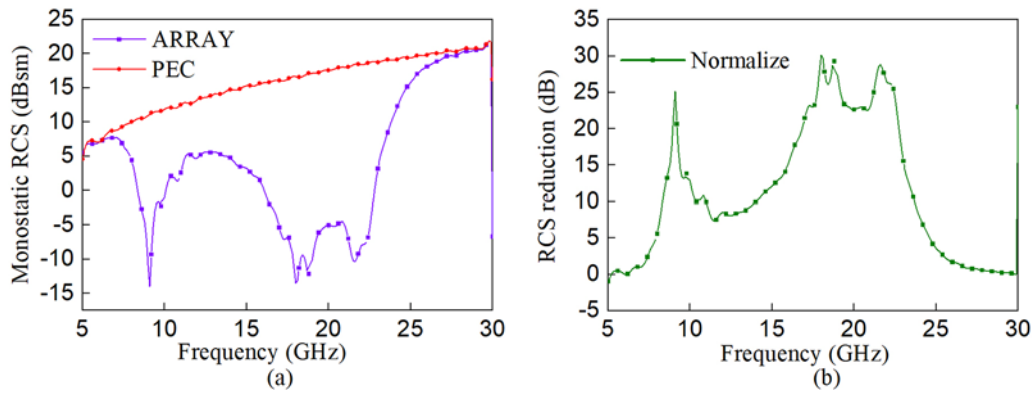


Figure 13. Simulated RCS: (a) monostatic RCS with respect to equal size PEC and (b) normalized monostatic RCS reduction.

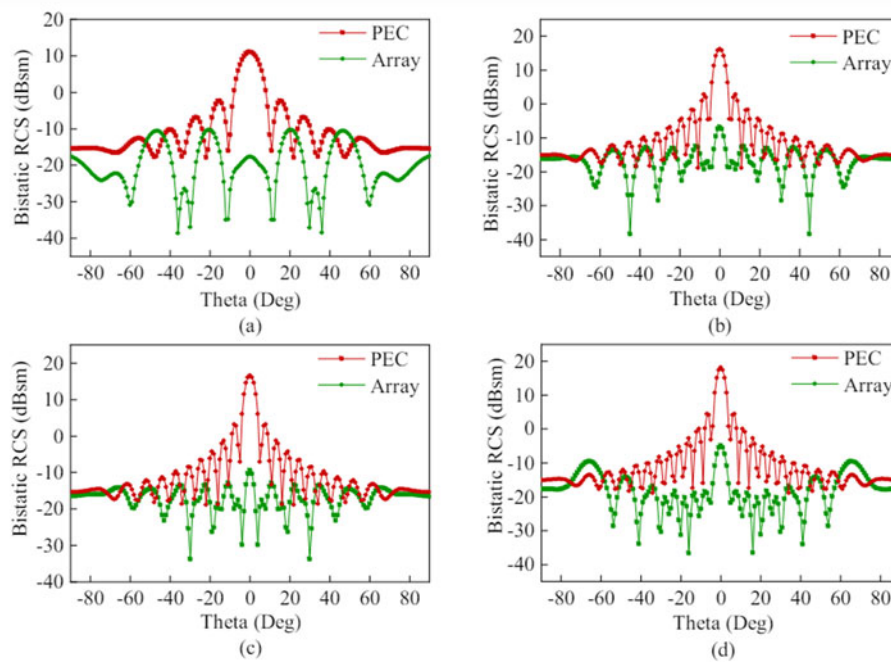


Figure 14. PEC and designed PCMS 2D scattering patterns at resonance frequencies: (a) 9.6, (b) 16.4, (c) 23.1, and (d) central frequency 15.6 (all in GHz).

understanding of how the various geometric parameters (p , h_s , w , and l) of the design unit cell affect its polarization conversion performance. Parametric analysis is performed by changing only one parameter of the design unit cell whereas the other parameters remain constant under normal incidence condition. The PCR and FBW of the design PCMS by changing various parameters are shown in Figure 10. It demonstrates that changing the unit cell parameters has a direct impact on PCR performance and bandwidth. Figure 10(a) indicates that reducing the length and width of the substrate (p) from 6.0 to 4.8 mm reduces PCR while increasing its FBW, and shifting performance toward higher frequencies because of the inverse relation between size and frequency. The parameter (h_s) represents substrate thickness, and it has also influenced the PCR and FBW of the design unit cell. The performance of the designed unit cell is evaluated for four different thicknesses of the F4BM substrate, i.e., $h_s = 3.0, 2.5, 2.0,$ and 1.5 mm, respectively. Figure 10(b) indicates that changing the thickness of the substrate (h_s) from 3.0 to 1.5 mm results in decreases of PCR and FBW, and the frequency band is shifting to higher frequencies. According

to Figure 10(c), the width (w) of the biconic shape resonator is reduced from 1.4 to 0.5 mm, which indicates that by reducing the width, the PCR increases while the FBW decreases. In Figure 10(d) by decreasing the length (l) of the resonator from 3.06 to 1.56 mm, it is observed that by decreasing the l , the PCR is decreasing on lower frequencies, its efficiency decreases and shifts the performance band to higher frequencies. So by changing any one of the parameter either PCR will increase or decrease, FBW will be decreased or increased and the band will be shifted toward higher or lower frequencies. The pink curves in Figure 10 indicate the final design unit cell performance.

RCS reduction with PCMS

RCS is the measure of a target's ability to reflect radar signals in the direction of the radar receiver. RCS is an important physical parameter to quantify the EM scattering ability of the targets. The RCS of the surface can be expressed as [36]:

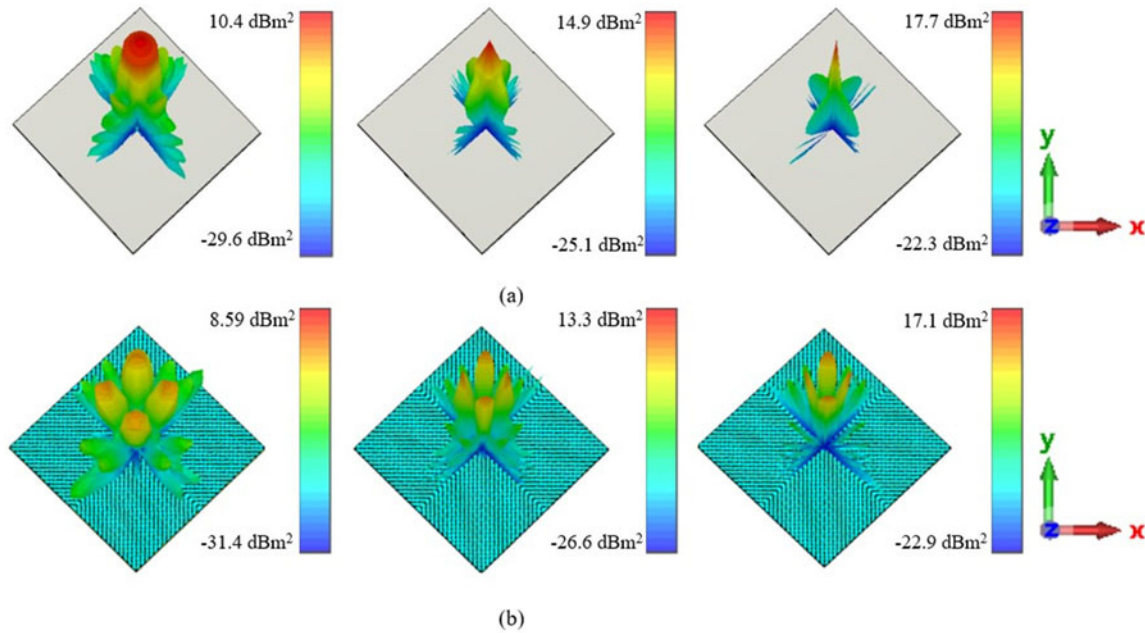


Figure 15. Simulated 3D scattering performance at 9.6 GHz, 16.4 GHz, and 23.1 GHz of (a) PEC and (b) the proposed chessboard array.

$$\sigma_c = 4\pi \lim_{r \rightarrow \infty} r^2 \frac{|\vec{E}_{rx}|^2}{|\vec{E}_{ix}|^2}. \tag{7}$$

The RCS reduction from the surface relative to the PEC can be expressed as [36]:

$$RCS\ reduction\ (dB) = 10 \log_{10} \left[\frac{\lim_{r \rightarrow \infty} 4\pi r^2 \frac{|\vec{E}_{rx}|^2}{|\vec{E}_{ix}|^2}}{\lim_{r \rightarrow \infty} 4\pi r^2 |1|^2} \right] \tag{8}$$

where σ_c denotes the RCS, $|E_{rx}|$ and $|E_{ix}|$ are the reflected and incident fields in the far zone of $r \rightarrow \infty$, respectively, and r is the detecting distance. As previously mentioned, a single-layer biconic shape PCMS is designed. The proposed PCMS is organized in chessboard orientations in this section to better understand its RCS reduction capability. A unit cell and its rotated version are required for the RCS reduction using polarization converting technique. The reflection coefficient of the mirror unit cell is depicted in Figure 11(a). The designed unit cell and its mirror unit cell have a cross-polarization $\Delta\varphi$ of 180° , which are necessary for RCS reduction as illustrated in Figure 11(b). The designed chessboard array simulation is performed in time domain using CST Microwave Studio (2020). A 30×30 square chessboard array with a total dimension of $168\text{ mm} \times 168\text{ mm}$ was designed based on the abovementioned unit cells. The chessboard array consists of four sub-arrays, each sub-array contains 15×15 unit cells. Two sub-arrays (1) contain the designed unit cell and the two sub-arrays (0) contain mirror unit cell as displayed in Figure 12. When a plane wave with y -polarized strikes the surface of the proposed square chessboard array, in which the unit cell reflects in-phase waves while its mirror reflects out phase waves, resulting in destructive interference (wave cancellation) and a reduction in RCS occur. Figure 13 presents the monostatic RCS of the proposed array compared to a PEC of the same size. According to the simulation results, the proposed chessboard array reduces more than

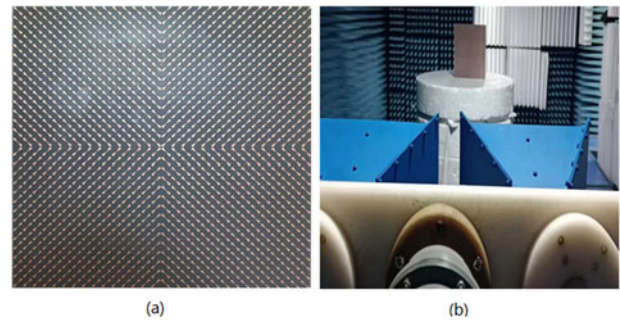


Figure 16. Images of (a) fabricated sample and (b) an experimental setup.

10 dB monostatic RCS throughout a large frequency range between 7.9 and 23.4 GHz with an FBW of 99%. The highest monostatic RCS reduction of the square chessboard array is -14 dB which is achieved at 9.6 GHz.

The simulated results of the 2D bistatic RCS for the proposed 30×30 square chessboard array under the normal incident at 9.6, 16.4, 23.1, and central frequency 15.6 GHz are depicted in Figure 14, which shows that the strength of the main lobes is decreased. At frequencies 9.6, 16.4, and 23.1 GHz, the proposed chessboard array's RCS reduction is about 28, 22, and 25 dB for normal incidence, less than the PEC maximum RCS respectively. The reduction in bistatic RCS is due to reflected EM waves (in-phase and out-phase wave) scattering into four directions rather than a single lobe reflection. The three-dimensional scattered radiation patterns of the bistatic RCS reduction of the proposed chessboard array and PEC of the same sized are depicted in Figure 15. In case of PEC, the incident wave reflect back in a single lobe in the source direction but in case of the proposed square chessboard array the incident wave is scattered into four sub-lobes at different directions due to destructive interference caused by the unit cell and its rotated version. Figure 15 indicates that the proposed chessboard

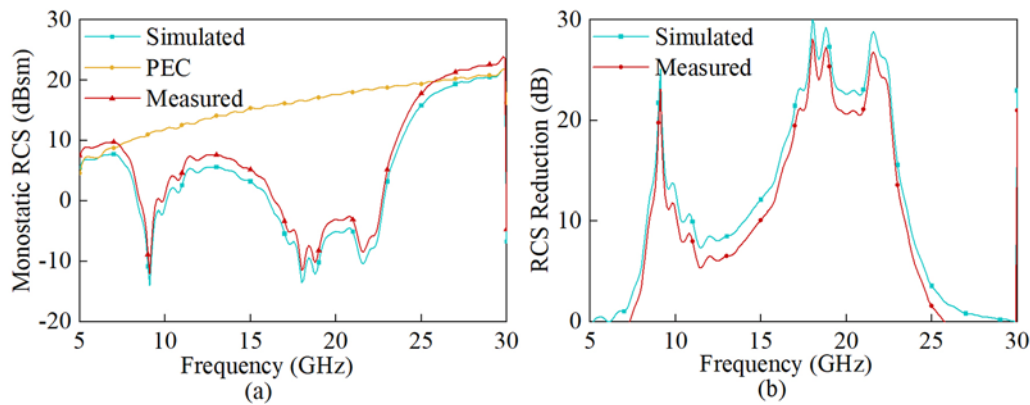


Figure 17. Comparison of the simulated and measured monostatic RCS results.

Table 1. Performance comparison of the square chessboard metasurface with previous research

Bandwidth (GHz)		Ref.	Size	Thickness	Relative bandwidth (%)	
PCR (90%)	RCS reduction (10 dB)				PCR	RCS reduction
7.2–22.5	8.2–21.5	[10]	$0.20\lambda_0$	$0.08\lambda_0$	101	89.5
8–13.5	7.7–13.7	[12]	$0.28\lambda_0$	$0.09\lambda_0$	51	56
9.2–17.6	9.2–17.6	[28]	$0.19\lambda_0$	$0.07\lambda_0$	62	62
10.6–21.1	8–23	[37]	$0.35\lambda_0$	$0.09\lambda_0$	65.7	96.7
11.7–19.8	10.5–20.5	[38]	$0.39\lambda_0$	$0.15\lambda_0$	51.4	64.5
10.2–22.6	8.75–24.0	[39]	$0.27\lambda_0$	$0.1\lambda_0$	75.6	95.4
9.5–18	9.92–19.8	[40]	$0.17\lambda_0$	$0.1\lambda_0$	61.8	66.8
10.8–17.9	5.5–16	[41]	$0.21\lambda_0$	$0.07\lambda_0$	49.4	76.2
8.7–24.8	7.9–23.4	Proposed	$0.16\lambda_0$	$0.07\lambda_0$	96	99

array has minimum reflection at the source direction as compared to PEC.

Fabrication and experimental results

The proposed 30×30 square chessboard array is fabricated in order to experimentally check the results of the simulation under the normal incidence. Figure 16(a) shows the fabricated prototype of the proposed square chessboard array. To test the proposed prototype, two horn antennas operating in 5–30 GHz band are positioned in the far field, 2 m from the surface. The two horns are connected to the KEYSIGHT N5224A vector network analyzer surrounded by absorbers, the wave is transmitted using one horn and received using the other as illustrated in Figure 16(b). Furthermore, the fabricated sample and the two horn antennas are aligned in monostatic RCS measurement. The measured results of the proposed prototype are compared to a similar sized PEC surface performances. Figure 17 displays a comparison of the measured results of the square chessboard array and simulation results. The developed metasurface measured and simulation results show good correlation over a wide frequency range, which validate that the developed PCMS attain wideband with effective RCS reduction. The performance comparison of our work with previously published works with respect to PCR and RCS bandwidth, size, thickness, and relative bandwidth is presented in Table 1. The PCR and RCS reduction bandwidth, relative bandwidth, of the proposed PCMS is greater than that of the comparable works. Also

the proposed PCMS has a small size than all the referenced work, and small thickness except [28, 41]. The proposed PCMS achieved wideband with a single resonator and in the all other references the wideband is achieved by using two or more resonators. In [10], double split-ring patches were used, in [12] Γ -shape is used, in [28] two oblique asymmetry triangle split rings are used, in [37] an I-shaped ring symmetrical structure is used, in [38] combination of a ring and a cross resonator are used, in [39] split-ring unit cell is used, in [40] N-shaped metallic pattern is used, in [41] periodic array of square patches, patch connected with ground through vias are used. These structures were developed using more metallic layers or a more complex pattern. The developed PCMS is constructed on a low cost, light-weight, and extremely thin F4BM substrate that makes it easier to use.

Conclusion

This study presents the design, analysis, fabrication, and an experimental measurement of the single-layer PCMS for wideband RCS reduction. The proposed PCMS is biconic-shape resonator, which convert the LP state of EM waves to their orthogonal polarization state. The proposed PCMS has PCR higher than 90% from 8.7 to 24.8 GHz; moreover, the proposed structure is applied in chessboard configuration, using phase cancellation techniques for RCS reduction. Results from the simulation and measurements indicate that the square chessboard array achieved RCS reduction of 10 dB in the operating bandwidth of 7.9–23.4 GHz except

for 10–15 GHz. A scattering pattern with four lobes is exhibited in the chessboard configuration which deviates from normal direction. Due to its low profile, wide bandwidth, and highly effective performance, the proposed PCMS has the ability to use in different application such as polarization control devices, imaging, radar invisibility, antenna system (gain enhancement and beam steering), remote sensing, and microwave communications.

Data availability statement. The data that support the findings of this study are available from the corresponding author upon reasonable request.

Funding statement. This research received no external funding.

Disclosure statement. No potential conflict of interest was reported by the authors.

References

1. **Abdullah M, Koziel S and Szczepanski S** (2021) Normalized partial scattering cross section for performance evaluation of low-observability scattering structures. *Electronics* **10**(14), 1731.
2. **Kamal B, Chen J, Yin Y, et al.** (2020) A broad band polarization converting metasurface for c and x-band applications. In *2020 IEEE International Conference on Signal Processing, Communications and Computing (ICSPCC)*. Hongkong: IEEE, pp. 1–4.
3. **Khan TA, Li J, Chen J, et al.** (2019) Design of a low scattering metasurface for stealth applications. *Materials* **12**(18), 3031.
4. **Xu J, Li R, Qin J, et al.** (2018) Ultra-broadband wide-angle linear polarization converter based on H-shaped metasurface. *Optics Express* **26**(16), 20913–20919.
5. **Zhang Z, Wang J, Fu X, et al.** (2021) Single-layer metasurface for ultra-wideband polarization conversion: Bandwidth extension via Fano resonance. *Scientific Reports* **11**(1), 1–8.
6. **Qi Y, Zhang B, Liu C, et al.** (2020) Ultra-broadband polarization conversion meta-surface and its application in polarization converter and RCS reduction. *IEEE Access* **8**(22), 116675–116684.
7. **Khan B, Ullah S, Kamal B, et al.** (2019) An extended split ring resonator type metasurface for microwave applications. In *2019 16th International Bhurban Conference on Applied Sciences and Technology (IBCAST)*. Islamabad, Pakistan: IEEE, pp. 1046–1049.
8. **Khan B, Kamal B, Ullah S, et al.** (2020) Design and experimental analysis of dual-band polarization converting metasurface for microwave applications. *Scientific Reports* **10**(1), 1–13.
9. **Bianmei Z, Chen W, Shuo Y, Xiaofan Y, Zhibin F, and Xiaoming L** (2023) Dual-band transmissive linear to circular polarization converter with angular-stable and orthogonal polarizations. *International Journal of Microwave and Wireless Technologies* **16**(3) 1–9.
10. **Mu X, Lv M and Ni T** (2022) Design of an ultra-broadband polarization rotating reflective surface for the reduction of radar cross section. *Progress in Electromagnetics Research M* **114**, 69–78.
11. **Hao H, Du S and Zhang T** (2019) Small-size broadband coding metasurface for RCS reduction based on particle swarm optimization algorithm. *Progress in Electromagnetics Research M* **81**, 97–105.
12. **Tiwari P, Pathak SK, Vp A, et al.** (2020) X-band Γ -shaped anisotropic metasurface-based perfect cross-polarizer for RCS reduction. *Journal of Electromagnetic Waves and Applications* **34**(7), 894–906.
13. **Wan X, Xiang Jiang W, Feng Ma H, et al.** (2014) A broadband transformation-optics metasurface lens. *Applied Physics Letters* **104**(15), 151601.
14. **Kamal B, Ullah S, Khan B, et al.** (2021) Ultrathin and high efficient wide-band polarization converting metasurface. *International Journal of RF and Microwave Computer-Aided Engineering* **31**(7), e22673.
15. **Tiwari P, Pathak SK, and Anitha V** (2021) Design, development and characterization of wide incidence angle and polarization insensitive metasurface absorber based on resistive-ink for X and Ku band RCS reduction. *Waves in Random and Complex Media* **34**(4) 1–16.
16. **Kamal B, Chen J, Yingzeng Y, et al.** (2021) High efficiency and ultra-wideband polarization converter based on an L-shaped metasurface. *Optical Materials Express* **11**(5), 1343–1352.
17. **Kamal B, Chen J, Yin Y, et al.** (2020) Wide band cross polarization converting metasurface based on circular split rings resonators. In *2020 IEEE International Conference on Computational Electromagnetics (ICCEM)*. Singapore: IEEE, pp. 223–225.
18. **Lin Bq, Huang W, Yang Y, et al.** (2022) An ultra-wideband polarization conversion metasurface for RCS reduction. *Journal of Electromagnetic Waves and Applications* **36**(5), 597–606.
19. **Ahmad T, Rahim AA, Bilal RMH, et al.** (2022) Ultrawideband cross-polarization converter using anisotropic reflective metasurface. *Electronics* **11**(3), 487.
20. **Fang C, Cheng Y, He Z, et al.** (2017) Design of a wideband reflective linear polarization converter based on the ladder-shaped structure metasurface. *Optik* **137**, 148–155.
21. **Ozturk G** (2022) Ultra-thin, wide-angle and bandwidth-enhanced linear and circular metasurface-based reflection-type polarization converter at X-band microwave frequency. *Journal of Electromagnetic Waves and Applications* **10**(10) 1–13.
22. **Li F, Chen H, Zhang L, et al.** (2018) Compact high-efficiency broadband metamaterial polarizing reflector at microwave frequencies. *IEEE Transactions on Microwave Theory and Techniques* **67**(2), 606–614.
23. **Deng G, Sun H, Lv K, et al.** (2020) An efficient wideband cross-polarization converter manufactured by stacking metal/dielectric multilayers via 3D printing. *Journal of Applied Physics* **127**(9), 093103.
24. **Xi Y, Jiang W, Hong T, et al.** (2021) Wideband and wide-angle radar cross section reduction using a hybrid mechanism metasurface. *Optics Express* **29**(14), 22427–22441.
25. **Su J, He H, Li Z, et al.** (2018) Uneven-layered coding metamaterial tile for ultra-wideband RCS reduction and diffuse scattering. *Scientific Reports* **8**(1), 1–9.
26. **Ameri E, Esmaeli SH and Sedighy SH** (2019) Ultra wideband radar cross section reduction by using polarization conversion metasurfaces. *Scientific Reports* **9**(1), 1–8.
27. **Ameri E, Esmaeli SH and Sedighy SH** (2018) Low cost and thin metasurface for ultra wide band and wide angle polarization insensitive radar cross section reduction. *Applied Physics Letters* **112**(20), 201601.
28. **Zheng Q, Guo C, Li H, et al.** (2018) Broadband radar cross-section reduction using polarization conversion metasurface. *International Journal of Microwave and Wireless Technologies* **10**(2), 197–206.
29. **Deng ZH, Wang FW, Ren YH, et al.** (2019) A novel wideband low-RCS reflector by hexagon polarization rotation surfaces. *IEEE Access* **7**, 131527–131533.
30. **Chatterjee J, Mohan A and Dixit V** (2021) Radar cross section reduction and gain enhancement of slot antenna using polarization conversion metasurface for X-band applications. *International Journal of RF and Microwave Computer-Aided Engineering* **31**(10), e22792.
31. **Kamal B, Chen J, Yin Y, et al.** (2022) Broad-band and broad-angle linear and circular polarization converting metasurface. *Journal of Electromagnetic Waves and Applications* **36**(8), 1102–1112.
32. **Kamal B, Khan B, Chen J, Yin Y, et al.** (2023) Ultra-thin wide-band polarization converting metasurface for complete KU and K bands microwave applications Zhengzhou, China: IEEE, 1–4. In *2023 IEEE International Conference on Signal Processing, Communications and Computing (ICSPCC)*.
33. **Yao M, Jianbo W, Lihua S, Shuyun X, Yuzhou R, Jie L and Yicheng L** (2021) Ultra-wideband, optically transparent, and flexible microwave metasurface absorber. *Optical Materials Express* **11**(7), 2206–2217.
34. **Priyanka T, Surya KP, and Siju V** (2022) Development of resistive-ink based planar and conformal metasurfaces for RCS reduction. *IEEE Access* **10**(2), 61472–61483
35. **Abbasi QH, Abbas HT, Alomainy A and Imran MA** (2021) *Backscattering and RF Sensing for Future Wireless Communication*. John Wiley & Sons.

36. **Fu C, Han L, Liu C, et al.** (2020) Dual-band polarization conversion metasurface for RCS reduction. *IEEE Transactions on Antennas and Propagation* **69**(5), 3044–3049.
37. **Lu J, Cao X, Gao J, et al.** (2021) Low RCS reflective polarization conversion metasurface. In *2021 International Conference on Microwave and Millimeter Wave Technology (ICMMT)*. Nanjing, China: IEEE, pp. 1–3.
38. **Zhang Z, Cao X, Gao J, et al.** (2018) Wideband radar cross section reduction using polarization conversion metasurface. In *2018 International Conference on Microwave and Millimeter Wave Technology (ICMMT)*. Chengdu, China: IEEE, pp. 1–3.
39. **Shu Y, Zhang Y, He S, et al.** (2018) An ultra-wideband metasurface for RCS reduction. In *2018 International Applied Computational Electromagnetics Society Symposium-China (ACES)*. Beijing, China: IEEE, pp. 1–2.
40. **Zheng Q, Li Y, Zhang J, et al.** (2017) Wideband, wide-angle coding phase gradient metasurfaces based on pancharatnam-berry phase. *Scientific Reports* **7**(1), 43543.
41. **Jia Y, Liu Y, Guo YJ, et al.** (2015) Broadband polarization rotation reflective surfaces and their applications to RCS reduction. *IEEE Transactions on Antennas and Propagation* **64**(1), 179–188.